Journal of Materials Science & Technology 164 (2023) 95–101

Contents lists available at ScienceDirect

Journal of Materials Science & Technology

journal homepage: www.elsevier.com/locate/jmst

Research Article

# Two-dimensional perovskite $Pb_2Nb_3O_{10}$ photodetectors

Yong Zhang[a,b,1], Jian Yao[b,1], Zhen Zhang[b], Rong Zhang[b], Li Li[b], Yu Teng[b], Zongjie Shen[b], Lixing Kang[b,*], Limin Wu[c,d,*], Xiaosheng Fang[c,*]

[a] School of Electronic and Information Engineering, Changshu Institute of Technology, Changshu 215500, China
[b] Division of Advanced Materials, Suzhou Institute of Nano-Tech and Nano-Bionics, Chinese Academy of Sciences, Suzhou 215123, China
[c] Department of Materials Science, State Key Laboratory of Molecular Engineering of Polymers, Fudan University, Shanghai 200433, China
[d] College of Chemistry and Chemical Engineering, Inner Mongolia University, Hohhot 010021, China

ARTICLE INFO

*Article history:*
Received 28 March 2023
Revised 23 May 2023
Accepted 29 May 2023
Available online 8 June 2023

*Keywords:*
$Pb_2Nb_3O_{10}$
Photodetectors
Self-powered
Two-dimensional
Perovskite

ABSTRACT

For the first time, we report high-performance two-dimensional (2D) perovskite $Pb_2Nb_3O_{10}$ photodetectors (PNO PDs). The few-layer PNO nanosheets are obtained successfully through a simple calcination and liquid exfoliation method. The individual PNO nanosheet devices with various structures (Au-PNO-Au, Au-PNO-Ti, Ti-PNO-Ti) are fabricated and investigated. The Au-PNO-Ti device exhibits a high rectification factor ($\sim 10^2$) owing to a large Schottky barrier difference between the PNO nanosheet and two asymmetric electrodes. Notably, the Au-PNO-Ti device shows excellent self-powered performance, including high responsivity (2.8 A/W), high detectivity ($1.1 \times 10^{12}$ Jones), and fast speed (0.2/1.2 ms) at 350 nm light illumination. This work not only suggests the performance of the PNO nanosheet PDs but also sheds light on the development of high-stability and high-performance devices based on 2D perovskite niobate in the future.



## 1. Introduction

Perovskites are a unique kind of ionic materials, including halide and oxide structures. The common chemical formula for perovskites is $ABX_3$, where A and B are all cations and X is a halide or an oxide anion. The replacement of ionic species leads to numerous perovskites with distinct characteristics and properties [1–3]. In the field of optoelectronic applications, halide perovskites ($ABI_3$) are excellent semiconductors owing to their remarkable optical and electrical properties, such as high absorption coefficients, long carrier-diffusion lengths, high carrier mobilities, and tunable bandgaps [4,5]. Therefore, the halide $ABI_3$ perovskites have important applications in the fields of photovoltaic, photoelectric detection, catalysis, and luminescence [6–12]. However, the B-I bond of halide $ABI_3$ perovskites is a single bond with a small band gap and weak bond energy. So the halide perovskites have poor stability, which limits their application conditions and fields. Conversely, the B-O bond of the oxide perovskite ($ABO_3$) is a double bond with a large band gap and strong bond energy. Oxide perovskites can be regarded as insulators with ultra-high stability, but their photoelectric performance is rarely mentioned. Oxide perovskites ($ABO_3$) display innumerous combinations of compounds with various physical and chemical properties, which have been used extensively in dielectric, ferroelectric, superconductivity, magnetic, catalytic, and energy devices [13–16]. Therefore, it is of great research value to explore and develop the application of oxide perovskites in the field of optoelectronics.

Layered oxide perovskites are important multifunctional materials, and have many interesting physical and chemical properties owing to strongly interacting d orbital electrons. Of particular interest is the two-dimensional (2D) oxide perovskite structures. Their diverse characteristics, usually very different from their bulk features, provide an outstanding platform for revealing novel paradigms in physics, chemistry, and innovative applications [17–20]. Nowadays, 2D perovskite niobate nanosheets exfoliated from layered bulk $AB_2Nb_3O_{10}$ have attracted extensive attention. By intercalating tetrabutylammonium hydroxide (TBAOH), the interlayer space of $AB_2Nb_3O_{10}$ can be swelled to the delamination point and therefore colloidal $(TBA^+)B_2Nb_3O_{10}$ nanosheets are successfully obtained. The perovskite $Pb_2Nb_3O_{10}$ (PNO) nanosheet is a kind of layered oxide perovskite with a Dion-Jacobson structure, as well as stable property, which makes PNO nanosheets a potential candidate for extensive applications. For example, previous studies have explored the high catalytic performance of $Pb_2Nb_3O_{10}$ nanosheets for hydrogen evolution and oxygen

* Corresponding authors.
*E-mail addresses:* lxkang2013@sinano.ac.cn (L. Kang), lmw@fudna.edu.cn (L. Wu), xshfang@fudan.edu.cn (X. Fang).
[1] These authors contributed equally to this work.

https://doi.org/10.1016/j.jmst.2023.05.011
1005-0302/

generation. The unique layered structure of the PNO nanosheets provided rich active sites and promotes the migration of reactants [21–23]. Meanwhile, in our recent work, 2D perovskite $Sr_2Nb_3O_{10}$ and $Ca_2Nb_3O_{10}$ UV photodetectors (PDs) were fabricated and demonstrated excellent UV detection capability [24–27]. In addition, the self-powered PDs attract much attention without an additional power supply [28–31]. However, little research has been conducted on PNO nanosheets, especially in the field of optoelectronics. Therefore, it is of great significance to explore efficient photodetection based on the perovskite $Pb_2Nb_3O_{10}$ nanosheets.

Herein, the 2D perovskite PNO nanosheets were successfully prepared via a high-temperature solid-state reaction, proton exchange, and liquid exfoliation process. The morphology, structure, crystallinity, and optical property of the PNO nanosheets were characterized in detail. In order to study its intrinsic characteristics, the individual few-layer PNO nanosheet devices (Au-PNO-Au, Ti-PNO-Ti, Au-PNO-Ti) were fabricated and investigated. Due to a large Schottky barrier difference between the PNO nanosheet and two asymmetric electrodes, the Au-PNO-Ti device exhibits a high rectification characteristic and demonstrates markedly different light responses at 3 V and −3 V. More importantly, this Au-PNO-Ti device shows high responsivity, high detectivity, and fast speed under 350 nm light illumination at zero bias voltage. Our work provides a new candidate for developing high-performance and high-stability photodetectors based on perovskite $Pb_2Nb_3O_{10}$ nanosheets in the future.

## 2. Experimental

### 2.1. Synthesis of $Pb_2Nb_3O_{10}$ nanosheets

The $Pb_2Nb_3O_{10}$ nanosheets were synthesized through typical calcination and exfoliation method. $RbPb_2Nb_3O_{10}$ was obtained through a conventional solid-state reaction. $Rb_2CO_3$, PbO, and $Nb_2O_5$ were mixed at a molar ratio of 1.2:4:3 with 20% excess $Rb_2CO_3$ to compensate for the loss owing to volatilization during the calcination process. The mixture was fully ground for one hour by adding alcohol. The mixture was then transferred into a corundum crucible and calcined in air at 1000 °C for 24 h. For sufficient solid-state reaction, the mixture was ground and calcined at 1000 °C for 24 h again. Subsequently, $RbPb_2Nb_3O_{10}$ and 5 M $HNO_3$ solution were shaken slowly for 5 days, with a renewal of the nitric acid solution every day. Then the protonated form ($HPb_2Nb_3O_{10}$) can be obtained. The $HPb_2Nb_3O_{10}$ products were washed and dried. The resulting $HPb_2Nb_3O_{10}$ products were shaken in TBAOH aqueous solution with an equimolar for 3 days to obtain the (TBA)$Pb_2Nb_3O_{10}$. Finally, a colloidal suspension of $Pb_2Nb_3O_{10}$ nanosheets was collected by centrifugation. Therefore, the $Pb_2Nb_3O_{10}$ nanosheets have high stability to temperature, acid, and alkali solutions. TBA+ molecules can be burned out under UV light exposure. The $[Pb_2Nb_3O_{10}]^-$ nanosheets can usually be abbreviated as $Pb_2Nb_3O_{10}$ (PNO).

### 2.2. Characterization of $Pb_2Nb_3O_{10}$ samples

The morphology and size of PNO nanosheets were investigated by field-emission scanning electron microscopy (Quanta 400 FEG, FEI). The thickness of PNO nanosheets was observed by a Bruker atomic force microscope (Dimension ICON). The high-resolution structure and morphology of PNO nanosheets were characterized by transmission electron microscopy (Tecnai G2 F20 S-TWIN). The crystal structure analysis of PNO samples was carried out by a Bruker D8 Advance diffractometer. The elemental composition of PNO nanosheets was conducted by X-ray photoelectron spectroscopy (XPS, PHI 5000 Versaprobell). The UV–vis spectroscopy for PNO nanosheets was measured by a UV–vis-IR spectrophotometer (Cary 5000).

### 2.3. Photoelectric measurements

The PNO nanosheet devices were fabricated by photolithography, deposition of metal electrodes (Au or Ti), and lift-off process. All the electric and photoelectric characteristics were measured by the Keithley 4200 semiconductor characterization system. A Xenon lamp with a monochromator was used as the light source, and its power density was conducted with a NOVA II power meter. The pulse response measurement was carried out by a digital oscilloscope and 355 nm Nd:YAG pulsed laser system. All the measurements were performed in the atmosphere at room temperature.

## 3. Results and discussion

The $Pb_2Nb_3O_{10}$ (PNO) nanosheets were prepared by a simple high-temperature solid-state sintering, proton exchange with nitric acid, and shaking-exfoliation in TBAOH aqueous solution. The scanning electron microscopy method (SEM) was utilized to investigate the corresponding products in each step, as shown in Fig. 1(a–c). The first step is the synthesis of $RbPb_2Nb_3O_{10}$ (RPNO) products via solid-state calcination. As exhibited in Fig. 1(a), the RPNO crystals are well-crystallized, and the lateral dimension of the large grains can reach up to a ten-micron level. RPNO displays a layered nature, leaving room for the next interlayer and exfoliation. Secondly, the $HPb_2Nb_3O_{10}$ (HPNO) products are obtained by replacing $Rb^+$ of RPNO products with $H^+$ in nitric acid, displaying a well-defined layered structure with some clearly visible cracks, as exhibited in Fig. 1(b). Finally, the PNO nanosheets are achieved by shaking the exfoliation process, and the $H^+$ can be exchanged with $TBA^+$ in TBAOH aqueous solution, as exhibited in Fig. 1(c). The size of PNO nanosheets ranges from 500 to 5000 nm. It is noteworthy that the average size of PNO nanosheets can be controlled through centrifugation at different speeds. The samples of low-speed centrifugation will be removed, and the samples of high-speed centrifugation are employed to characterize and fabricate devices. In addition, the energy-dispersive X-ray spectroscopy (EDS) mapping method was utilized to investigate the elements distribution of PNO nanosheets. Fig. S1 in the Supplementary Material shows the transmission electron microscopy (TEM) image of the PNO nanosheets for the EDS mapping pattern. Fig. 1(d–f) exhibits the EDS mapping images of the PNO nanosheets. It can be observed that Pb (Fig. 1(d)), Nb (Fig. 1(e)), and O (Fig. 1(f)) are distributed evenly for the PNO nanosheets. Due to the thick thickness of the PNO nanosheet, many sampling points are displayed. Therefore, 2D PNO nanosheets are successfully achieved and can be dispersed in ethanol or deionized water with long-term stability. This simple, large-scale, and low-cost preparation of PNO nanosheets is conducive to constructing scaled-up devices.

The morphology, structure, and crystalline phase of PNO nanosheets were further characterized by the TEM analysis. As shown in Fig. 2(a), the size of the PNO nanosheets is observed clearly in low magnification TEM. Many PNO nanosheets with different thicknesses are stacked together, and some nanosheets are almost transparent, indicating that the thickness of the PNO nanosheets is very thin. The high-resolution TEM (HRTEM) pattern in Fig. 2(b) displays the distances between planes in both vertical directions, which are measured as 0.39 nm, corresponding to the (100) and (010) planes of PNO nanosheets. As seen in Fig. 2(c), the distinct diffraction spots from selected area electron diffraction (SAED) measurements prove the high quality of PNO nanosheet crystals. The labeled spots are indexed as (010) and (100) planes, respectively, indicating the zone axis as [001]. Furthermore, Fig. 2(d) shows the 3D structural diagram of a mono-

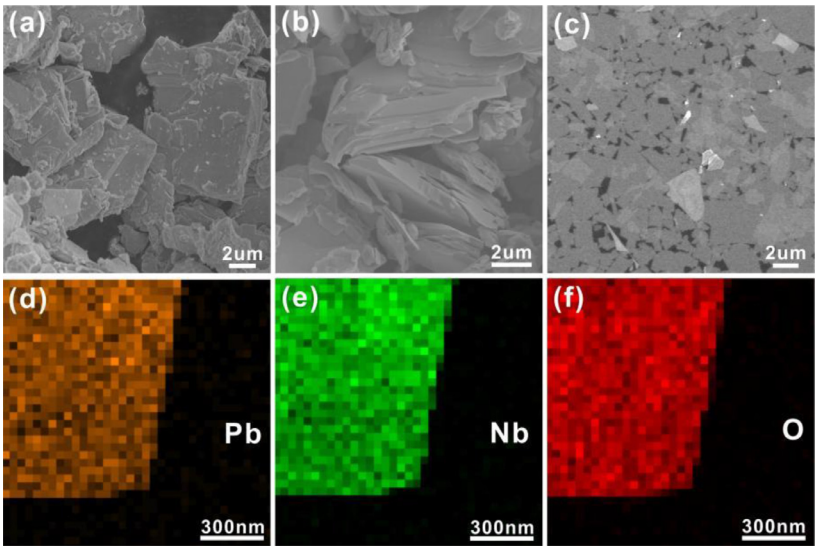


**Fig. 1.** Morphology and elemental composition of PNO nanosheets. (a–c) SEM images of RPNO samples after calcination, HPNO samples after proton exchange, and PNO nanosheets after liquid exfoliation, respectively. (d–f) EDS mapping images of Pb, Nb, and O elements, respectively.

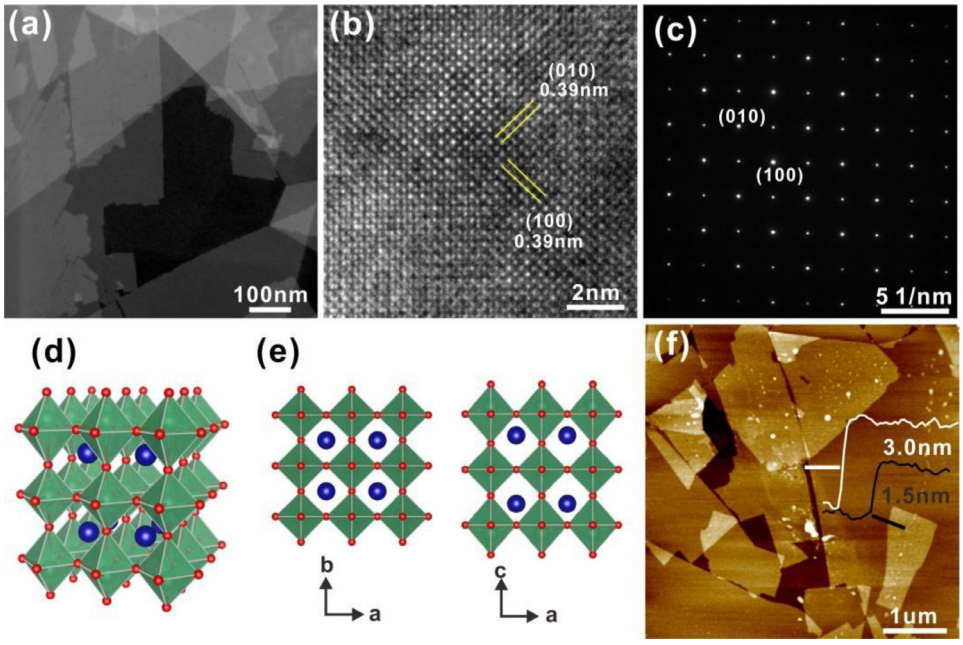


**Fig. 2.** Structure and morphology of PNO nanosheets. (a–c) TEM image, HRTEM image, and SAED pattern of PNO nanosheets, respectively. (d, e) Schematic illustration of the 3D and 2D structure for monolayer PNO nanosheet. (f) AFM image of PNO nanosheets and insert presents the height profiles.

layer PNO crystal, where three $NbO_6$ octahedral lamellae share corners to form a single-layer PNO nanosheet. The 2D structural illustration of the PNO crystal is clearly observed in Fig. 2(e), and the *c*-axis is along [001] zone axis direction. The *c*-axis in Fig. 2(e) is equivalent to the [001] axis in Fig. 2(c). Additionally, according to the atomic force microscope pattern (AFM) in Fig. 2(f). The thickness of a single-layer CNO nanosheet with three $NbO_6$ octahedra lamellae is measured as 1.5 nm. The thickness of the two-layer PNO nanosheet is measured as 3.0 nm from the height profiles. Therefore, monolayer or few-layer PNO nanosheets have ultrathin thicknesses and good dispersion, which are convenient for their combination with different substrates.

To investigate the phase structure of samples throughout the whole preparation process, the X-ray diffraction technique (XRD) was employed to study corresponding products after high-temperature reaction, proton exchange, and exfoliated PNO nanosheets, respectively. As exhibited in Fig. 3(a–c), the crystal phases of products substantially change during the three experimental steps. As a common Dion-Jacobson perovskite, RPNO is built by negative $[Pb_2Nb_3O_{10}]^-$ nanosheets and interlayer dispersive $Rb^+$, and the XRD pattern of RPNO is exhibited as the comparison in Fig. 3(a). The HPNO samples display single-phase diffraction patterns in Fig. 3(b). And the HPNO samples were indexed to a structure of stacked perovskite slabs with a tetragonal unit cell ($a$ = 0.39 nm, $c$ = 1.5 nm), which is consistent with Refs. [21,22]. The characteristic diffraction peaks at 5.8°, 11.6°, 28.3°, 32.2°, and 46.5° corresponded to (001), (002), (103), (110), and (200) planes, respectively. The (001) and (002) diffraction peaks from $(TBA/H)Pb_2Nb_3O_{10}$ nanosheets were also observed in Fig. 3(c), suggesting that the structure of perovskite crystal slabs in HPNO remained unchanged during the exfoliation process. It is worth noting that the relative intensity of the (00l) peak for

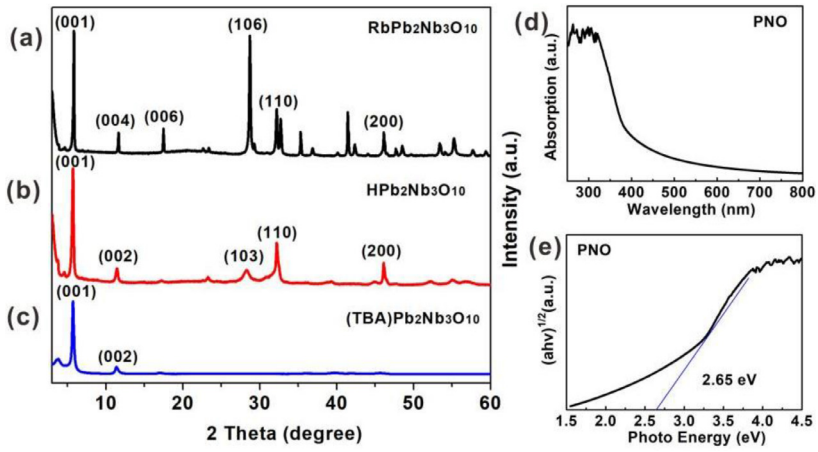


**Fig. 3.** (a–c) XRD patterns of RPNO samples after calcination, HPNO samples after proton exchange, and PNO nanosheets after liquid exfoliation, respectively. (d, e) UV–vis absorption spectrum and the corresponding Tauc curve of the PNO nanosheets, respectively.

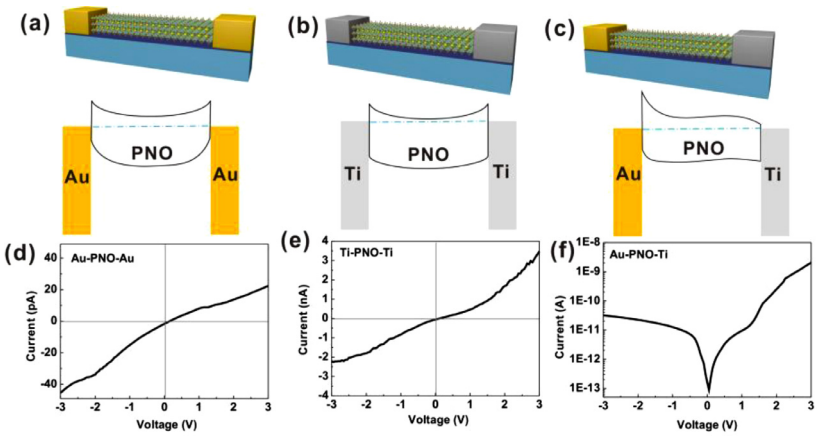


**Fig. 4.** The PNO nanosheet devices based on the Schottky junction. (a–c) The structures and energy band diagrams for PNO devices with different metal electrodes. (d–f) Typical *I–V* characteristics of PNO devices with different contacts, respectively.

(TBA/H)$Pb_2Nb_3O_{10}$ nanosheets is considerably weaker than that of HPNO, indicating that the periodic layered structure was destroyed upon the intercalation and exfoliation. The structural information of PNO nanosheets by XRD pattern agrees with the TEM results. Meanwhile, the chemical state and surface elemental composition of the exfoliated PNO nanosheets were confirmed by X-ray photoelectron spectroscopy (XPS), as illustrated in Fig. S2. In addition, the optical property of PNO nanosheets was measured. As shown in Fig. 3(d), the PNO nanosheets exhibit gradual absorption in the visible area and an obvious absorption edge near 450 nm from the UV–vis absorption spectrum. As seen in Fig. 3(e), the optical bandgap was calculated as 2.65 eV by the Tauc plots. The few-layer PNO nanosheets with high crystallinity are beneficial for investigating their photoelectric properties.

To investigate the Schottky junction characteristics of PNO nanosheets, the individual PNO nanosheet diodes with different metal contacts were fabricated by typical photolithography, deposition of metal electrodes, and lift-off method. The asymmetric Schottky junction based on PNO nanosheets was also achieved successfully by constructing asymmetric metal contacts. As seen in Fig. 4(a–c), three different devices with metal-semiconductor-metal contact electrodes (Au-PNO-Au, Ti-PNO-Ti, Au-PNO-Ti) and corresponding energy band descriptions were investigated, respectively. Au and Ti with work functions of 5.1 and 4.3 eV were selected as metal electrodes, respectively. The barrier height of the Schottky junction can be simply expressed as the difference between the metal work function and the electron affinity of the semiconductor. A Schottky barrier difference can be produced between Au-PNO and Ti-PNO interfaces. Therefore, the main depletion area is formed mainly on the PNO-Au interface to yield a built-in electric field. When the PNO device is irradiated with incident light, photon-generated carriers can be separated effectively through the built-in electric field without an additional power supply to produce photocurrent.

To evaluate the junction between a single PNO nanosheet and metal electrodes, several metal-semiconductor-metal devices based on PNO nanosheets were fabricated with Au and Ti contact electrodes. As seen in Fig. 4(d–f), the *I–V* curves of the fabricated Au-PNO-Au, Ti-PNO-Ti, and Au-PNO-Ti devices under dark conditions were measured, respectively. The dark current ($I_d$) of a device can reveal the rectifying characteristic of the Schottky contact. The thermionic emission diffusion theory of a Schottky junction can be employed to describe the *I–V* features. Therefore, the $I_d$ through a metal-semiconductor junction can be given as follows:

$$I_d = AA * T^2 \exp(\frac{-\Phi_B}{kT}) \exp(\frac{qV}{nkT}) \quad (1)$$

In the equation, $A$ and $A^*$ represent the effective contact area and the Richardson constant, $\Phi_B$, and $q$ denote the Schottky barrier height and elementary charge, $k$ and $T$ refer to Boltzmann constant and absolute temperature, $V$ and $n$ are the applied bias and the ideality factor of 1, respectively. Fig. 4(d) displays the *I–V* curve from Au-PNO-Au contact, revealing a lower dark current and displaying a back-to-back Schottky contact characteristic. The

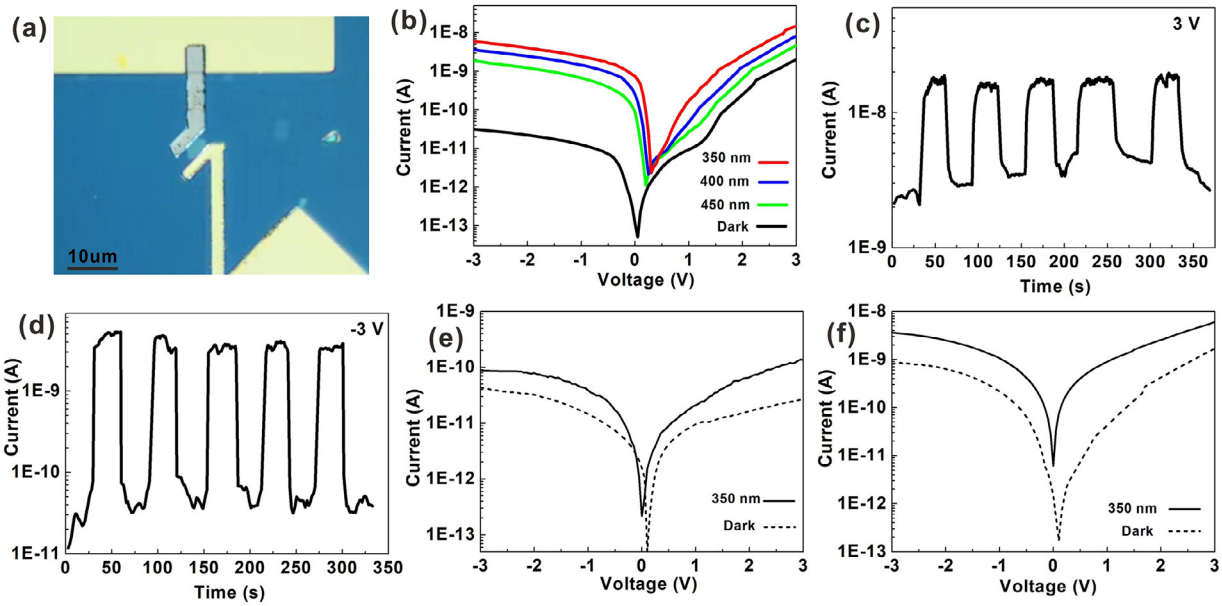


**Fig. 5.** Photodetecting performance of the Au-PNO-Ti device. (a) Optical microscope photograph of the Au-PNO-Ti device. (b) *I–V* curves of the Au-PNO-Ti device under different light illumination. (c, d) *I–t* curves of the Au-PNO-Ti device at 350 nm at 3 V and –3 V, respectively. (e, f) *I–V* curves of the Au-PNO-Au (e) and Ti-PNO-Ti (f) devices at 350 nm, respectively.

Schottky barrier height for Au-PNO contact can be calculated as 0.59 eV by fitting the linear region from the *I–V* curve. As for the Ti-PNO junction, a larger current reveals a smaller Schottky junction (0.46 eV) between Ti and PNO (Fig. 4(e)). As for the Au-PNO-Ti device, the *I–V* curve shows typical diode characteristic (Fig. 4(f)), and the diode displays a high rectification factor of ~100 (2.0 nA @ 3 V; 21 pA @ –3 V). Additionally, to eliminate the differences of the as-prepared PNO nanosheets by aqueous solution exfoliation process, *I–V* curves of another three Au-PNO-Ti devices were also carried out. As displayed in Fig. S3, these devices exhibit similar rectification behaviours based on different PNO nanosheets. The PNO nanosheets are obtained by the liquid exfoliation process and have different shapes, sizes, and thicknesses. Therefore, the different Au-PNO-Ti nanosheet devices are fabricated and investigated, and exhibit different electronic properties. These results indicate that the PNO Schottky junction can be successfully fabricated by utilizing Au and Ti contacts, which provides additional possibilities for fabricating self-powered photodetectors based on PNO nanosheets.

To explore its photoelectric properties and self-powered features, the Au-PNO-Ti devices were constructed with different metal contacts (Au and Ti) by a twice lithography process. The photoelectric properties of the Au-PNO-Ti devices were carried out using a two-probe technique at room temperature. Fig. 5(a) exhibits the optical photograph of an individual PNO nanosheet PDs with Au and Ti electrodes. Fig. S4 displays the optical microscope photographs of three other PNO nanosheet devices with asymmetric metal contacts. Fig. 5(b) displays the typical current–voltage (*I–V*) curves of an Au-PNO-Ti device in a logarithmic plot in the dark and under different light irradiation. The *I–V* features of the Au-PNO-Ti device indicate the rectifying characteristic, revealing the successful formation of the asymmetric Schottky junction. Especially, the Au-PNO-Ti device displays a large on-state at the reverse bias and a small on-state at the forward bias. The photodiode exhibits a rectification factor of 100 at ± 3 V, similar to the Au-InSe-In photodiode in Ref. [32]. The high rectification factor of this photodiode may be attributable to the high quality of the interface between the PNO nanosheet and metal contacts.

As displayed in Fig. 5(b), the photoresponse of the Au-PNO-Ti device can be observed clearly under different light illuminations. An obvious enhancement in photocurrent can be seen and the photocurrent can reach 6.0 nA at –3 V under 350 nm light irradiation, which is much higher than the dark current at the reverse bias of –3 V and lower than photocurrent (14 nA) at the forward bias of 3 V. Notably, the photocurrent of the Au-PNO-Ti device is up to 200 times that of its dark current (30 pA) at –3 V, and is as low as 7 times that of its dark current (2 nA) at 3 V under 350 nm light illumination. In particular, an evident shift of the *I–V* feature indicates the generation of an open-circuit voltage (~0.25 V) from the Au-PNO-Ti device under different light illumination. It is worth noting that the noticeable difference between the photocurrent and dark current at zero bias indicates the possible self-powered characteristic of the Au-PNO-Ti device. Therefore, this Au-PNO-Ti device exhibits typical photodiode characteristics and displays different photoresponse performances at different bias voltages. The PNO Schottky junction device formed between two asymmetric electrodes indicates great potential for work in a self-powered feature.

In order to further explore the photoelectric performance, the current–time (*I–t*) features of the Au-PNO-Ti device at –3 V and 3 V were measured, respectively. As displayed in Fig. 5(c, d), the Au-PNO-Ti device both shows a stable and reproducible photoresponse under 350 nm light irradiation at 3 V and –3 V. However, the Au-PNO-Ti device displays significantly different photoelectric performance at –3 V and 3 V owing to their different on-states. As the light is switched on and off, the current of this Au-PNO-Ti PD increases rapidly to 17 nA and decreases rapidly to 3.5 nA at 3 V, while the current increases quickly to 3.8 nA and declines quickly to 42 pA at –3 V. The on/off ratio of a device is described as the ratio of the photocurrent to the dark current ($I_{ph}/I_d$). By contrasting the results, it is found that the Au-PNO-Ti PD at –3 V displays slightly a lower photocurrent (3.8 nA) and a much larger on-off ratio (90) than that of 17 nA and 5 at 3 V, respectively. In addition, the Au-PNO-Au and Ti-PNO-Ti devices were also fabricated and measured, respectively. As shown in Fig. 5(e, f), the *I–V* features of the Au-PNO-Au and Ti-PNO-Ti PDs in dark conditions and under light illumination exhibit nearly symmetrical characteristics. This suggests that the symmetrical Schottky barrier between Au (or Ti) electrodes and the PNO nanosheet is difficult to produce the

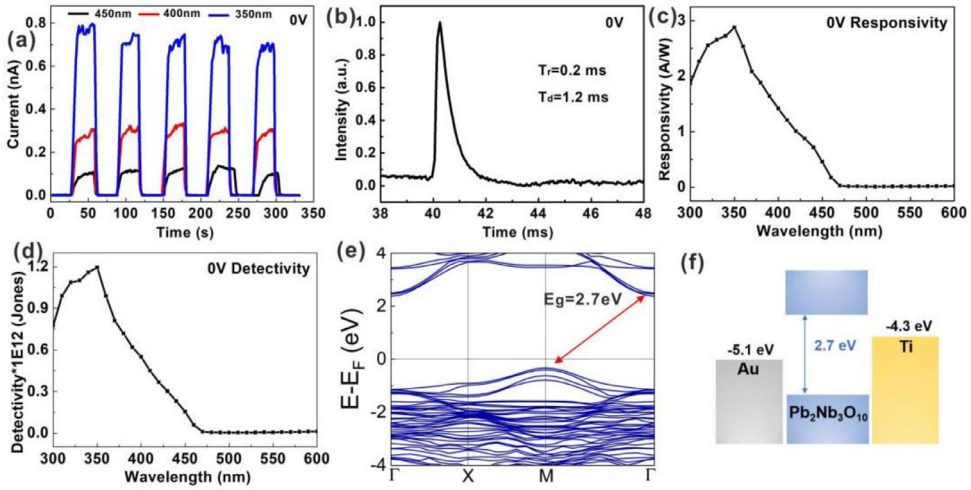


**Fig. 6.** Photodetecting performance of the Au-PNO-Ti device at 350 nm at 0 V. (a) *I–t* curves for the device under different light illumination. (b) The normalized pulse response of the device. (c, d) The responsivity and detectivity for the Au-PNO-Ti device, respectively. (e) Electronic band structure of monolayer HPNO nanosheet. (f) Band alignment of the Au-PNO-Ti device.

self-powered performance. As seen in Fig. S5, the Ti-PNO-Ti device displays a much higher photocurrent than that of the Au-PNO-Au device owing to a relatively low barrier height. The built-in electric field is mainly produced on the PNO-Au interface and can be used as the driving force to separate electron-hole pairs in light irradiation and generate a stable photocurrent without any power supply. Therefore, the Au-PNO-Ti device displays clearly different photoelectric performances at 3 V and −3 V separately and may operate at different biases to realize multifunctional detection. These results confirm that the Au-PNO-Ti device not only has the ability to detect light in the UV–vis region but also indicates potential self-powered performance.

To evaluate the self-powered performances of the Au-PNO-Ti device, it was measured at zero voltage bias upon 350 nm light irradiation, and the results were exhibited in Fig. 6. The repeatability of a photodetector is an important parameter to assess its performance. Fig. 6(a) displays the *I–t* curves of the Au-PNO-Ti device at 0 V under different light illumination. These curves exhibit good reproducibility and fast photo-response without delay. The photocurrent of the Au-PNO-Ti device remains stable under continuous light irradiation at 0 V, indicating that the built-in electric field can efficiently work without an external power source. When the light is switched on and off, the photocurrent of the Au-PNO-Ti device increases quickly to 0.1, 0.3, and 0.7 nA and quickly decreases to the initial state (1.0 pA) under 450, 400, and 350 nm light illumination, respectively. The on-off ratios of the Au-PNO-Ti PD are measured as 100, 300, and 700, respectively. To evaluate the response time accurately, fast response measurement equipment was employed for the Au-PNO-Ti device. Fig. 6(b) displays the normalized feature of the pulse response as a function of time at 0 V using a 355 nm pulsed laser. The rise time can be described as the peak of photocurrent ascending from 10% to 90%. The decay time can be described as the peak of photocurrent descending from 90% to 10%. The rise and decay times are measured to be 0.2 and 1.2 ms for the Au-PNO-Ti PD, respectively. The surface state of the PNO nanosheet may block carrier transport and recombination, thereby producing a long decay time. Therefore, the PNO device exhibits good repeatability, a high photocurrent (0.7 nA), a large on-off ratio (700), and a fast speed (0.2 and 1.2 ms) at zero bias at 350 nm light illumination, demonstrating its great potential in the development of microscale photodetectors.

The spectral responsivity ($R_\lambda$) and detectivity ($D^*$) are two crucial parameters for evaluating the self-powered property of the Au-PNO-Ti device. The responsivity describes as the photocurrent per unit of incident light intensity, revealing how efficiently a device responds to light signals. The detectivity ($D^*$, typically defined as Jones) represents the ability to detect weak light signals from the surrounding noise environment. The major contribution of background noise is to act as the shot noise in the dark current. The responsivity and detectivity of a detector can be defined as the following equation [33,34]:

$$R_\lambda = \left(I_{ph} - I_d\right)/(P_\lambda S) \tag{2}$$

$$D^* = R_\lambda/(2eI_d/S)^{1/2} \tag{3}$$

where $I_{ph}$ and $I_d$ represent photocurrent and dark current, e and λ represent the electronic charge and irradiation light wavelength, and $P_\lambda$ and $S$ represent the light power density and the effective light illumination area, respectively. Fig. 6(c, d) exhibits the spectral responsivity ($R_\lambda$) and specific detectivity ($D^*$) of the Au-PNO-Ti device for the incident light wavelength ranging from 600 to 300 nm at zero bias, respectively. As displayed in Fig. 6(c), the maximum responsivity of the Au-PNO-Ti device is 2.8 A/W at 350 nm light illumination, demonstrating high detecting sensitivity to the UV light signals. It is found that the responsivity quickly increases near 450 nm, which corresponds to the bandgap of the PNO nanosheet. As seen in Fig. 6(d), the detectivity of the Au-PNO-Ti device displays a similar changing trend to responsivity with the wavelength ranging from 600 to 300 nm at 0 V. Due to the low dark current and the high responsivity, the detectivity of this device can reach up to $1.1 \times 10^{12}$ Jones at 350 nm light irradiation at 0 V.

The electronic band structure of the monolayer HPNO nanosheet is calculated by density functional theory, and the result is exhibited in Fig. 6(e). In fact, the interior of the few-layered PNO nanosheets inevitably contains H ions. So the calculation of the monolayer HPNO nanosheet is reasonable [35]. The HPNO nanosheet is found to have an indirect band gap of 2.7 eV, which is in good agreement with the experimental value. The relative positions of the different work functions for the Au-PNO-Ti device are illustrated in Fig. 6(f). Under dark conditions, PNO and Au (Ti) have different Fermi energies formation before contact with each other. The contact of PNO with Au and Ti results in different Schottky barriers at the interfaces. The formation of a depletion region by the Schottky barrier mainly occurs at the Au-PNO

interface, which introduces a built-in field. Subsequently, the generation and separation of electron-hole pairs could produce a stable photocurrent during light illumination. These results demonstrate that the Au-PNO-Ti device exhibits excellent self-powered performances, including a high on-off ratio (700), fast speed (0.2/1.2 ms), high responsivity (2.8 A/W), and high detectivity ($1.1 \times 10^{12}$ Jones). Meanwhile, the PNO nanosheets were prepared on a large scale via a simple and low-cost calcination-exfoliation method. In addition, the PNO nanosheets have long-term stability, far superior to most 2D materials and halide perovskites. Therefore, the PNO nanosheets may be a promising candidate for practical optoelectronic applications.

## 4. Conclusions

In summary, 2D perovskite PNO nanosheets were prepared successfully via a high-temperature solid-state reaction, proton exchange, and liquid exfoliation method. The PNO nanosheets were characterized by SEM, AFM, TEM, HRTEM, and XRD, which showed their high crystallinity and thicknesses down to 1.5 nm. The individual few-layer PNO nanosheet devices (Au-PNO-Au, Ti-PNO-Ti, and Au-PNO-Ti) with different electrode configurations were fabricated and investigated. In particular, the Au-PNO-Ti device exhibits a high rectification behavior ($\sim 10^2$) owing to a large Schottky barrier difference between the PNO nanosheet and two asymmetric electrodes. More notably, this Au-PNO-Ti device demonstrates excellent self-powered performance, including high responsivity (2.8 A/W), high detectivity ($1.1 \times 10^{12}$ Jones), and fast speed (0.2/1.2 ms) under 350 nm light illumination. This work not only suggests the high performance of the PNO nanosheet photodetectors but also sheds light on the development of high-stability and high-performance devices based on 2D perovskite niobate in the future.

## Declaration of Competing Interest

The authors declare that they have no known competing financial interests or personal relationships that could have appeared to influence the work reported in this paper.

## Acknowledgements

This work was supported by the National Natural Science Foundation of China (No. 52272136), the Natural Science Foundation of Jiangsu Province (No. BK20221402), and the China Postdoctoral Science Foundation (No. 2022M712322). The authors are grateful for the technical support for Nano-X from Suzhou Institute of Nano-Tech and Nano-Bionics, Chinese Academy of Sciences (SINANO).

## Supplementary materials

Supplementary material associated with this article can be found, in the online version, at doi:10.1016/j.jmst.2023.05.011.

## References

[1] A.G. Ricciardulli, S. Yang, J.H. Smet, M. Saliba, Nat. Mater. 20 (2021) 1325–1336.
[2] C.W. Sun, J.A. Alonso, J.J. Bian, Adv. Energy Mater. 11 (2021) 2000459.
[3] X.M. Xu, Y.L. Pan, Y.J. Zhong, R. Ranc, Z.P. Shao, Mater. Horiz. 7 (2020) 2519–2565.
[4] M. Ghasemi, B. Guo, K. Darabi, T.H. Wang, K. Wang, C.W. Huang, B.M. Lefler, L. Taussig, M. Chauhan, G. Baucom, T. Kim, E.D. Gomez, J.M. Atkin, S. Priya, A. Amassian, Nat. Mater. 22 (2023) 329–337.
[5] R.X. Lin, J. Xu, M.Y. Wei, Y.R. Wang, Z.Y. Qin, Z. Liu, J.L. Wu, K. Xiao, B. Chen, S.M. Park, G. Chen, H.R. Atapattu, K.R. Graham, J. Xu, J. Zhu, L.D. Li, C.F. Zhang, E.H. Sargent, H. Tan, Nature 603 (2022) 73–78.
[6] S. Chen, H.J. Yin, P.R. Liu, Y. Wang, H.J. Zhao, Adv. Mater. 35 (2023) 2203836.
[7] Y.Y. Zhou, L.M. Herz, A.K.Y. Jen, M. Saliba, Nat. Energy 7 (2022) 794–807.
[8] A. Fakharuddin, M.K. Gangishetty, M. Abdi-Jalebi, S.H. Chin, A.R.B. Mohd Yusoff, D.N. Congreve, W. Tress, F. Deschler, M. Vasilopoulou, H.J. Bolink, Nat. Electron. 5 (2022) 203–216.
[9] X.Y. He, Y. Deng, D.C. Ouyang, N. Zhang, J. Wang, A.A. Murthy, I. Spanopoulos, S.M. Islam, Q. Tu, G.C. Xing, Y. Li, V.P. Dravid, T.Y. Zhai, Chem. Rev. 123 (2023) 1207–1261.
[10] Y.L. Li, H.X. Sunb, Z. Li, M. Wang, L.Q. Guo, L.L. Minb, F.R. Cao, Y.Q. Tana, L. Li, J. Mater. Sci. Technol. 130 (2022) 35–43.
[11] X. He, M. Wang, F.R. Cao, W. Tian, L. Li, J. Mater. Sci. Technol. 124 (2022) 243–251.
[12] Y.H. Yun, H. Cho, J. Jung, S.W. Yang, D. Vidyasagar, R.K. Gunasekarana, S. Lee, J. Mater. Sci. Technol. 152 (2023) 100–108.
[13] Y. Okazaki, Y. Fujita, H. Murata, N. Masuyama, Y. Nojima, H. Ikeno, S. Yagi, I. Yamada, Chem. Mater. 34 (2022) 10973–10981.
[14] W.J. Yin, B.C. Weng, J. Ge, Q.D. Sun, Z.Z. Li, Y.F. Yan, Energy Environ. Sci. 12 (2019) 442–462.
[15] J.K. Huang, Y. Wan, J.J. Shi, J. Zhang, Z.H. Wang, W.X. Wang, N. Yang, Y. Liu, C.H. Lin, X.W. Guan, L. Hu, Z.L. Yang, B.C. Huang, Y.P. Chiu, J. Yang, V. Tung, D.Y. Wang, K. Kalantar-Zadeh, T. Wu, X.T. Zu, L. Qiao, L.J. Li, S. Li, Nature 605 (2022) 262–267.
[16] P.J. Xue, H. Wu, Y. Lu, X.H. Zhu, J. Mater. Sci. Technol. 34 (2018) 914–930.
[17] A.J. Yang, K. Han, K. Huang, C. Ye, W. Wen, R.X. Zhu, R. Zhu, J. Xu, T. Yu, P. Gao, Q.H. Xiong, X.R. Wang, Nat. Electron. 5 (2022) 233–240.
[18] J.L. Lu, W. Luo, J.S. Feng, H.J. Xiang, Nano Lett. 18 (2018) 595–601.
[19] J.E. ten Elshof, H.Y. Yuan, P.G. Rodriguez, Adv. Energy Mater. 6 (2016) 1600355.
[20] D.X. Ji, S.H. Cai, T.R. Paudel, H.Y. Sun, C.C. Zhang, L. Han, Y.F. Wei, Y.P. Zang, M. Gu, Y. Zhang, W.P. Gao, H.X. Huyan, W. Guo, D. Wu, Z.B. Gu, E.Y. Tsymbal, P. Wang, Y.F. Nie, X.Q. Pan, Nature 87 (2019) 87–92.
[21] B.T. Zheng, L.H. Mao, J.W. Shi, Q.Y. Chen, Y.C. Hu, G.Q. Zhang, J.T. Yao, Y.J. Lu, Int. J. Hydrog. Energy 46 (2021) 34276–34286.
[22] Y.C. Hu, J.W. Shi, L.J. Guo, Appl. Catal. A Gen. 468 (2013) 403–409.
[23] Y.C. Hu, L.J. Guo, ChemCatChem 7 (2015) 584–587.
[24] S.Y. Li, Y. Zhang, W. Yang, H. Liu, X.S. Fang, Adv. Mater. 32 (2020) 1905443.
[25] Y. Zhang, S.Y. Li, Z.L. Li, H. Liu, X.Y. Liu, J.X. Chen, X.S. Fang, Nano Lett. 21 (2021) 382–388.
[26] Y. Zhang, F. Cao, S.Y. Li, X.Y. Liu, L.X. Kang, L.M. Wu, X.S. Fang, J. Mater. Sci. Technol. 129 (2022) 108–114.
[27] X.Y. Liu, S.Y. Li, Z.Q. Li, Y. Zhang, W. Yang, Z.L. Li, H. Liu, D.V. Shtansky, X.S. Fang, Adv. Funct. Mater. 31 (2021) 2101480.
[28] T.T. Yan, Z.Q. Li, F. Cao, J.X. Chen, L.M. Wu, X.S. Fang, Adv. Mater. 34 (2022) 2201303.
[29] Y. Zhang, W.L. Liu, Y.S. Liu, C.H. Wang, G.D. Zhu, W.D. Song, J. Mater. Chem. C 9 (2021) 15654–15661.
[30] Y. Zhang, H. Liu, S. Liu, Q. Gong, Y.S. Liu, D. Tian, L.X. Kang, J. Mater. Chem. C 11 (2023) 127–133.
[31] W.J. Cheng, W. Tian, F.R. Cao, L. Li, InfoMat 4 (2022) e12348.
[32] M.J. Dai, H.Y. Chen, R. Feng, W. Feng, Y.X. Hu, H.H. Yang, G.B. Liu, X.S. Chen, J. Zhang, C.Y. Xu, P.A. Hu, ACS Nano 12 (2018) 8739–8747.
[33] L. Su, T.T. Yan, X.Y. Liu, F. Cao, X.S. Fang, Adv. Funct. Mater. 33 (2023) 2214533.
[34] Y.H. Chen, L.X. Su, M.M. Jiang, X.S. Fang, J. Mater. Sci. Technol. 105 (2022) 259–265.
[35] P.T. Xu, T.J. Milstein, T.E. Mallouk, ACS Appl. Mater. Interfaces 8 (2016) 11539–11547.